JOURNAL OF GEOPHYSICAL RESEARCH: PLANETS, VOL. 118, 321–334, doi:10.1002/jgre.20047, 2013

Vertical distribution of dust and water ice aerosols from CRISM limb-geometry observations

Michael D. Smith,[1] Michael J. Wolff,[2] R. Todd Clancy,[2] Armin Kleinböhl,[3] and Scott L. Murchie[4]

Received 31 May 2012; revised 14 November 2012; accepted 18 December 2012; published 27 February 2013.

[1] Near-infrared spectra taken in a limb-viewing geometry by the Compact Reconnaissance Imaging Spectrometer for Mars (CRISM) on board the Mars Reconnaissance Orbiter provide a useful tool for probing atmospheric structure. Specifically, the observed radiance as a function of wavelength and height above the limb enables the vertical distribution of both dust and water ice aerosols to be retrieved. More than a dozen sets of CRISM limb observations have been taken so far providing pole-to-pole cross sections, spanning more than a full Martian year. Radiative transfer modeling is used to model the observations taking into account multiple scattering from aerosols and the spherical geometry of the limb observations. Both dust and water ice vertical profiles often show a significant vertical structure for nearly all seasons and latitudes that is not consistent with the well-mixed or Conrath-ν assumptions that have often been used in the past for describing aerosol vertical profiles for retrieval and modeling purposes. Significant variations are seen in the retrieved vertical profiles of dust and water ice aerosol as a function of season. Dust typically extends to higher altitudes (~40–50 km) during the perihelion season than during the aphelion season (<20 km), and the Hellas region consistently shows more dust mixed to higher altitudes than other locations. Detached water ice clouds are common, and water ice aerosols are observed to cap the dust layer in all seasons.

Citation: Smith, M. D., M. J. Wolff, R. T. Clancy, A. Kleinböhl, and S. L. Murchie (2013), Vertical distribution of dust and water ice aerosols from CRISM limb-geometry observations, *J. Geophys. Res. Planets*, *118*, 321–334, doi:10.1002/jgre.20047.

1. Introduction

[2] The vertical distribution of aerosols in the Martian atmosphere is of great interest because it plays a large role in the vertical distribution of solar energy in the atmosphere and therefore controls heating rates throughout the atmosphere [*Gierasch and Goody*, 1972]. The vertical distribution of aerosols is also sensitive to many physical processes, including dynamics, transport, condensation microphysics, surface-atmosphere interaction, and photochemistry, and so it provides sensitive tests and constraints for a wide variety of models.

[3] In the past, a number of retrieval algorithms (e.g., [*Smith*, 2004, 2009]) have used the simplifying assumption that dust is well mixed with the background atmosphere. Although partially a computational necessity, this assumption was mostly imposed because nadir-viewing observations provide limited information about vertical structure. These studies have produced a very useful first look at the climatology of Mars aerosols, but it has also been known for some time that, at least under some conditions, dust and especially water ice aerosols are not well mixed, and recent work (e.g., [*Guzewich et al.*, 2011; *Richardson et al.*, 2011; *Rothchild et al.*, 2011]) has demonstrated that using a more realistic vertical profile for aerosol instead of the traditional simplified expressions leads to notable improvements between the modeled and the observed thermal structure.

[4] Observations taken at a geometry viewing the limb enable the vertical distribution of aerosols to be determined, but until recently, such retrievals have been relatively few in number. Images from orbit of the Martian limb by Mariner 9 [*Anderson and Leovy*, 1978], Viking [*Jaquin et al.*, 1986] and the Mars Global Surveyor (MGS) MOC [*Cantor*, 2007] cameras show that the haze associated with dust extends much higher above the surface during dust storms than when the atmosphere is less dusty. Observations of the Martian limb taken in a solar occultation geometry taken by Phobos [*Chassefière et al.*, 1992] and by the Mars Express SPICAM instrument [*Montmessin et al.*, 2006; *Rannou et al.*, 2006] show detached layers of water ice clouds

[1]NASA Goddard Space Flight Center, Greenbelt, Maryland, USA.
[2]Space Science Institute, Boulder, Colorado, USA.
[3]Jet Propulsion Laboratory, Pasadena, California, USA.
[4]Applied Physics Laboratory, The Johns Hopkins University, Laurel, Maryland, USA.

Corresponding author: M. D. Smith, NASA Goddard Space Flight Center, Greenbelt, MD 20771, USA. (Michael.D.Smith@nasa.gov)

2169-9097/13/10.1002/jgre.20047

superimposed on a background dust haze layer that varies in depth with season.

[5] In the past few years, a more complete characterization of the vertical distribution of aerosols has been compiled using limb-geometry observations by MGS Thermal Emission Spectrometer (TES) [*McConnochie and Smith*, 2008; *Clancy et al*., 2010] and Mars Reconnaissance Orbiter (MRO) Mars Climate Sounder (MCS) [*McCleese et al*., 2007, 2010; *Kleinböhl et al*., 2009, 2011; *Heavens et al*., 2011]. The retrievals from these observations have revealed the vertical distribution of aerosols over the course of the Martian year, including during great dust storms. Findings show that detached water ice clouds are common and that there are often significant departures of dust vertical distribution that are well mixed during the northern spring and summer seasons in the tropics.

[6] Near-infrared spectra returned by the MRO Compact Reconnaissance Imaging Spectrometer for Mars (CRISM) [*Murchie et al*., 2007, 2009] taken in the limb-viewing geometry provide another good source of information about the vertical distribution of dust and water ice aerosols. These observations, taken every few months, serve as an important complement to the aerosol profiling provided by the MRO MCS instrument by allowing independent validation and giving additional information on particle physical and scattering properties through multi-wavelength studies. CRISM limb observations have also been used to study other atmospheric phenomena such as O_2 airglow [*Clancy et al*., 2012].

[7] In this paper, we present the results of retrievals of the vertical distribution of dust and water ice aerosols in the Martian atmosphere using limb-geometry spectra taken by the CRISM instrument over more than one full Martian year. In section 2, we discuss the CRISM instrument and limb-viewing data set. Details of the retrieval algorithm are given in section 3. In section 4, we present the results of the retrievals, and those results are discussed and compared with other observations in section 5.

2. Data Set

[8] The MRO arrived at Mars in March 2006, completed aerobraking in August 2006, and began its primary science phase in November 2006; it continues to operate in its extended mission at the time of this writing. MRO operates from a Sun-synchronous, near-polar, near-circular (~300 km altitude) orbit with a mean local solar time of about 3:00 A.M./P.M. [*Zurek and Smrekar*, 2007].

2.1. CRISM Instrument and Limb Observations

[9] CRISM is a hyperspectral imager with a nadir spatial resolution of 15–19 m/pixel and a spectral range of 362–3920 nm with a spectral sampling of 6.55 nm and a spectral resolution in the near-infrared (~2000 nm) of about 10–15 nm [*Murchie et al*., 2007, 2009]. A gimbal allows off-nadir pointing in the fore or aft direction along track, and spacecraft roll allows off-nadir pointing in the across-track direction. There are two detector arrays each with 640 spatial pixels across track and 480 spectral pixels. One detector covers visible to near-infrared wavelengths (362–1056 nm), while the other covers infrared wavelengths (1001–3920 nm). Hyperspectral images are built up using a combination of orbital motion and gimbal movements.

[10] Observations of the limb are not a nominal observation for CRISM because the range of gimbal motion does not allow the limb to be observed in the nominal spacecraft nadir-pointing orientation. However, as a special observation, the spacecraft is occasionally oriented so that CRISM is able to observe either the forward or aft limb. During each opportunity for CRISM limb observations, the instrument is commanded to repeatedly scan upward and downward across the limb. Each *limb scan* thus consists of a spectral image cube with one spatial dimension parallel to the limb and one spatial dimension perpendicular to the limb. The limb observations are taken in a mode that averages 10 pixels in each spatial direction, which provides a spatial sampling at the limb tangent point of roughly 800 m. We further average the central 40 pixels in the direction parallel to the limb to increase signal-to-noise ratio with minimal impact on vertical resolution. Each limb scan includes coverage from below the limb to a tangent point at least 100 km above the limb. Limb observations are always taken in the full hyperspectral mode of the CRISM instrument.

[11] All of the limb scans taken during one particular special observation opportunity form a *limb set*. Each limb set nominally contains about 50 scans across the limb acquired pole to pole during two orbits at roughly 100°W and 290°W longitude, over the Tharsis and Syrtis Major/Hellas regions, respectively. At each longitude, limb scans are spaced roughly 10° in latitude. Figure 1 shows a map giving the latitude and longitude locations of a typical set of CRISM limb observations. Beginning with the most recent limb set taken in April 2012, a third orbit with an equator crossing at 0° longitude was added to the nominal two orbits shown in Figure 1.

[12] The first CRISM limb set was taken in July 2009, and additional limb sets have been added semi-regularly roughly every 2 to 4 months. As of this writing, a total of 15 limb sets have been obtained, spanning more than one Martian year (Table 1). Figure 2 gives a graphical representation of the seasonal coverage. All seasons are represented although there are fewer limb scans in southern spring/northern fall. An additional CRISM limb set taken in August 2010, or Mars year (MY) 30, solar longitude (L_s) = 137°, is not used in this study because a problem with the CRISM coolers during the observation resulted in loss of most useable data in the near-infrared portion of the CRISM spectral coverage (>1000 nm).

[13] At the near-infrared wavelengths used in this study, there is negligible contribution from thermal radiation, so we rely on scattered solar light for signal from aerosols. This means that we cannot view the winter polar regions or at

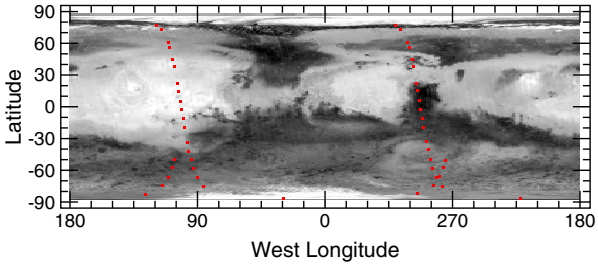

Figure 1. The latitude and longitude locations (small red squares) of CRISM limb scans for a limb set taken in July 2009 (MY 29, L_s = 301°). A typical limb set contains pole-to-pole coverage at two longitudes at approximately 100°W and 290°W. Other CRISM limb sets have similar distribution.

Table 1. Dates of CRISM Limb Sets

Earth Date	Mars Date and Season
10–11 July 2009	MY 29, $L_s = 301°$
10–11 February 2010	MY 30, $L_s = 50°$
7 April 2010	MY 30, $L_s = 74°$
28–29 April 2010	MY 30, $L_s = 84°$
26 May 2010	MY 30, $L_s = 96°$
22–24 August 2010	MY 30, $L_s = 137°$
17 October 2010	MY 30, $L_s = 166°$
5–6 December 2010	MY 30, $L_s = 193°$
31 March to 1 April 2011	MY 30, $L_s = 265°$
14–15 May 2011	MY 30, $L_s = 293°$
28 June 2011	MY 30, $L_s = 319°$
22–23 August 2011	MY 30, $L_s = 349°$
13 September 2011	MY 31, $L_s = 0°$
10–11 December 2001	MY 31, $L_s = 41°$
24–26 April 2012	MY 31, $L_s = 102°$

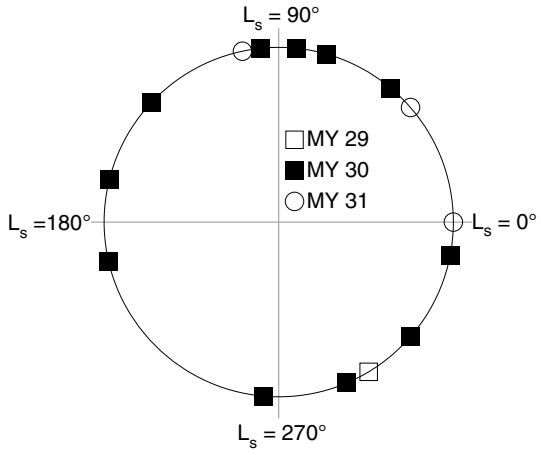

Figure 2. The seasonal dates of all CRISM limb sets. The observations span more than one Martian year, and all seasons are represented.

night. For adequate solar illumination and signal-to-noise ratio, we restrict our retrievals to limb scans with a solar incidence angle of 85° or less.

2.2. Typical CRISM Limb Set Spectra

[14] A typical limb scan is shown in Figure 3 (MY 29, $L_s = 301°$, 19°S latitude). An average of 40 10X-binned pixels parallel to the limb is included in each spectrum, and for clarity, only every tenth averaged spectrum (perpendicular to the limb) is shown. The spectra with the lowest tangent height (purple) are essentially the same as the nadir-geometry spectra, except for stronger gas absorptions due to the longer atmospheric path length. As the tangent height increases (blue, green, yellow, red), the observed signal gradually falls to zero. The overall "continuum" level is produced by the scattering of sunlight from aerosols, and numerous absorptions from atmospheric gases (primarily CO_2) are clearly visible. In this case, the continuum level falls monotonically to zero as tangent height increases, but in some cases, strong layering of aerosols causes an increase in observed signal with height. The continua fall to a

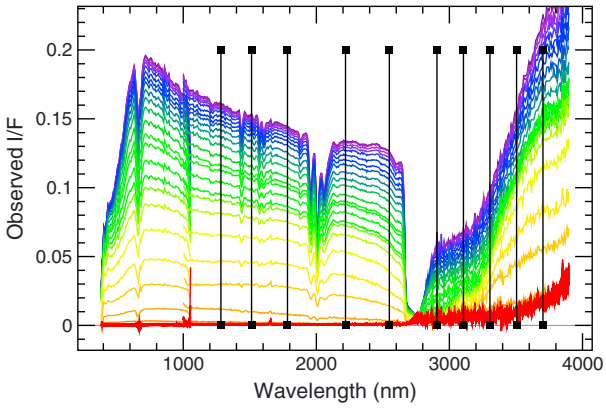

Figure 3. A typical CRISM limb scan from the limb set taken in July 2009 (MY 29, $L_s = 301°$, 19°S latitude, 290°W longitude). Color indicates tangent height above the surface, from purple (0 km) to red (50 km). The black vertical lines indicate the 10 wavelengths used to retrieve aerosol vertical profiles.

nonzero value at wavelengths greater than 3400 nm because of unremoved thermal emission inside the instrument.

3. Retrieval Algorithm

[15] The variation of the observed continuum signal as a function of wavelength and tangent height is used to retrieve the vertical profiles of dust and water ice aerosols. Dust and water ice are distinguished by the difference of their spectral variations of extinction and scattering properties using a set of 10 spectral channels that avoid the gas absorptions and are widely spaced across the CRISM spectrum (black vertical lines in Figure 3).

[16] Radiative transfer modeling of CRISM spectra has been used to retrieve the vertical distribution of dust and water ice aerosols. The basic idea is to vary the two profiles until a best fit is achieved between the computed and the observed spectrum as a function of tangent height at the 10 selected wavelengths. This process is explained in more detail below.

3.1. Radiative Transfer and Retrieval Process

[17] The near-infrared light observed by CRISM comes from aerosol scattering of sunlight into the line of sight of the instrument. The light can either be scattered directly from the solar beam or from sunlight reflected off the surface. Therefore, the observed signal is sensitive to both aerosol optical depth (and its vertical distribution) and surface albedo. At these wavelengths, thermal radiation is negligible, and the observed signal does not depend on atmospheric or surface temperature.

[18] Because aerosol scattering is dominant, full multiple scattering must be included in the radiative transfer modeling. In addition, the limb-viewing geometry requires that the spherical geometry inherent in the observations also be explicitly treated. However, a fully spherical radiative transfer code with multiple scattering is extremely computationally expensive. As a result, we choose a middle ground that combines efficiency and an approximate, though accurate, treatment of the spherical geometry that allows for relatively rapid retrievals.

The code has been extensively tested and validated against an "exact" Monte Carlo code [*Whitney et al.*, 1999; *Wolff et al.*, 2006] and found to be accurate within a few percent over a wide range of conditions and viewing geometries.

[19] The forward radiative transfer model uses the discrete ordinates method to treat multiple scattering [e.g., *Goody and Yung*, 1989; *Thomas and Stamnes*, 1999]. The atmosphere is divided into vertical layers, and the number of radiation "streams" can be set as high as necessary to accurately model the angular dependence of scattering. We use 50 atmospheric layers, each with a 0.2 scale height (~2 km) thickness, and 64 streams (32 pairs) to describe the radiation field. Atmospheric state variables (temperature, gas abundance, aerosol abundance, aerosol scattering properties, etc.) are specified separately for each vertical layer.

[20] Aerosol size is taken from careful modeling of the spectral dependence of dust absorption in TES spectra [*Wolff and Clancy*, 2003] and from multiwavelength comparisons of TES, mini-TES, and CRISM spectra [*Clancy et al.*, 2003; *Wolff et al.*, 2006, 2009]. Based on these analyses, we have chosen a single particle size distribution that is used for all the retrievals, with effective radius $r_{\text{eff}} = 1.5\,\mu$m for dust and $r_{\text{eff}} = 2.0\,\mu$m for water ice aerosols. Aerosol scattering properties are taken from a detailed modeling of CRISM emission phase function spectra, where the same spot on the surface is observed at a number of different emission angles as the spacecraft flies overhead [*Wolff et al.*, 2009]. Figure 4 shows the extinction efficiency and single-scattering albedo as a function of wavelength in the CRISM spectral range for this choice of dust and water ice and the different spectral character of the two aerosols over the wavelengths chosen for the retrieval (Figure 3).

[21] The spherical geometry is treated by computing the diffuse radiation field in a standard plane-parallel geometry using the discrete ordinates approach but then integrating the source functions along the equivalent curved path through the layers. As illustrated in Figure 5, the curved path is defined by computing the correct limb-geometry emission angle for the path at the boundary of each layer. This is often called the "pseudo-spherical approximation" [e.g., *Spurr*, 2002; *Thomas and Stamnes*, 1999] and is at least two orders of magnitude faster than a typical Monte Carlo computation. Figure 6 shows a comparison of our pseudo-spherical model against an exact Monte Carlo code. The pseudo-spherical model is generally accurate to within a few percent over a wide range of conditions.

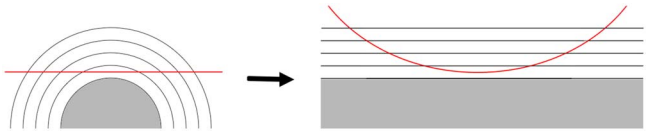

Figure 5. In the pseudo-spherical approximation, (left) limb viewing in the spherical geometry (red line) is approximated using (right) a curved path in a plane-parallel geometry. The emission angle at each layer boundary in the spherical geometry is accurately computed and used to compute the equivalent curved path.

[22] The retrieval algorithm finds the model parameters that provide the best fit in a chi-squared sense between the observed data (radiance at 10 wavelengths as a function of height above the limb) and the radiance computed from the forward radiative transfer model. The minimization of chi-square is accomplished using the nonlinear Levenberg-Marquardt routine found in *Press et al.* [1992]. In our experience, we have found this routine to be reasonably fast and extremely robust.

[23] The quantities retrieved are the vertical profiles of dust and water ice aerosols and the effective Lambert albedo of the surface at the 10 wavelengths used. The dust and water ice aerosol vertical profiles are each specified just above the surface and then every 0.4 pressure scale heights between 0.2 and 6.6 scale heights above the surface. This typically gives coverage up to at least 60 km above the surface with a vertical resolution <5 km. Together with the 10 surface albedos, there are 46 parameters retrieved. All

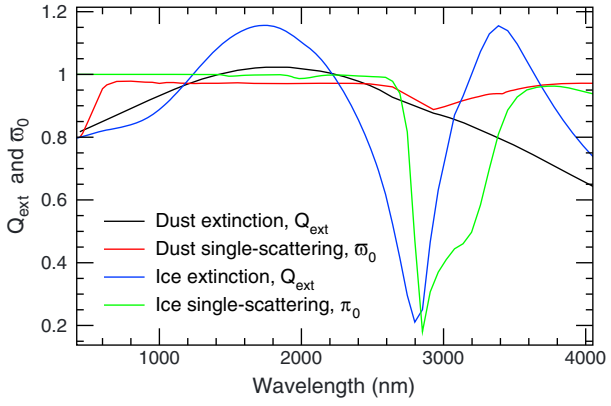

Figure 4. The extinction coefficient, Q_{ext}, and single-scattering albedo, $\bar{\omega}_0$, for dust and water ice aerosols used in this retrieval. The extinction coefficient has been scaled to unity at the reference wavelength of 2219 nm. These scattering properties are based on the analysis of TES and CRISM observations [*Wolff and Clancy*, 2003; *Clancy et al.*, 2003; *Wolff et al.*, 2009] and are representative of a mean particle size of 1.5 μm for dust and 2.0 μm for water ice aerosols.

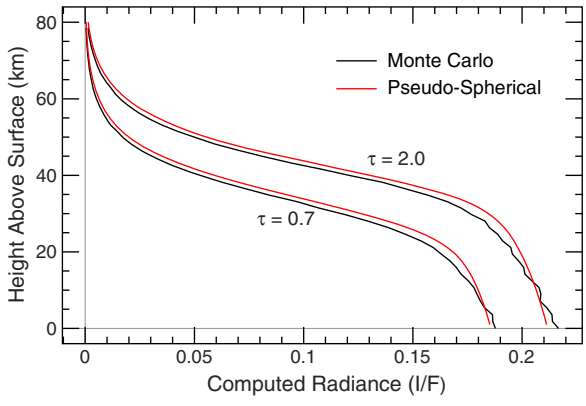

Figure 6. A comparison of computed radiance at a wavelength of 1 μm in the limb geometry between the "exact" Monte Carlo results (black lines) and the pseudo-spherical approximation (red lines) for two different column optical depths of dust aerosol, $\boldsymbol{\tau}$. The pseudo-spherical approximation is accurate to within a few percent over a wide range of conditions and is two orders of magnitude faster than the Monte Carlo calculation.

observations with tangent heights between 5 and 60 km are included in the retrieval, providing approximately 500 total observations over the 10 wavelengths. The viewing geometry, including the incidence angle, emission angle, phase angle, and distance between Mars and the Sun, is taken from spacecraft records and is assumed to be well known. The solar spectrum used is that adopted by the CRISM team, which is taken from the terrestrial MODTRAN atmospheric radiation code [*Berk et al.*, 1998].

3.2. Output Quantities

[24] The final output from the retrieval process are 18 point vertical profiles for dust and water ice aerosol opacity and the equivalent Lambert albedo at each of the 10 wavelengths used in the retrieval. These quantities are output to a file along with additional data describing the quality of the fit for each parameter.

[25] The aerosol opacities are given in terms of an aerosol "mixing ratio" that expresses the optical depth of dust or water ice across a model layer in terms of the atmospheric mass in that layer. This effectively divides out the exponential variation of atmospheric density with height and allows the vertical structure of aerosols to be seen more easily. In this representation, the total column optical depth, τ, can be found by summing the aerosol mixing ratio in each layer weighted by the mass in the layer:

$$\tau(\lambda) = \sum_{i=1}^{\text{layers}} n_i Q_{\text{ext}}(\lambda) \Delta p_i / p_{\text{surf}}, \quad (1)$$

where the sum is performed over all levels, n_i is the aerosol (dust or water ice) mixing ratio, and Q_{ext} is the extinction coefficient, which is a function of wavelength, λ. The ratio of the difference in atmospheric pressure across the model layer, Δp_i, to the surface pressure, p_{surf}, is equivalent to the fraction of the column mass contained within a particular layer. Surface pressure is retrieved from each CRISM limb scan in a separate step after the aerosol retrieval using the CO_2 band near 2000 nm. There is a separate mixing ratio, n_i, for each aerosol, dust and water ice. In the simple case of a well-mixed aerosol, the mixing ratio is constant for all levels, i, and the column optical depth is simply the product of the mixing ratio and the wavelength-dependent extinction coefficient. In this paper, we reference all mixing ratio values for both dust and water ice to a wavelength of 2219 nm, which is one of the wavelengths used in the retrieval near the center of the spectral range. Equivalently, we have scaled the extinction coefficient for both dust and water ice to be unity at 2219 nm, as shown in Figure 4.

[26] At a tangent height where the line-of-sight aerosol optical depth becomes significantly greater than unity, the retrieval becomes insensitive to variations in the aerosol vertical distribution below that level. Figure 7 shows the relative sensitivity of observed signal, *I/F*, to a change in aerosol mixing ratio as a function of height. Each line shows the response to adding an increment of dust aerosol to a single layer in the model (the results are similar for water ice aerosol). For the relatively clear case with column optical depth 0.4, there is sensitivity to changes in the aerosol vertical profile down to approximately 10 km above the surface. However, at times with high dust or water ice optical depth, the retrieval is valid over a more restricted

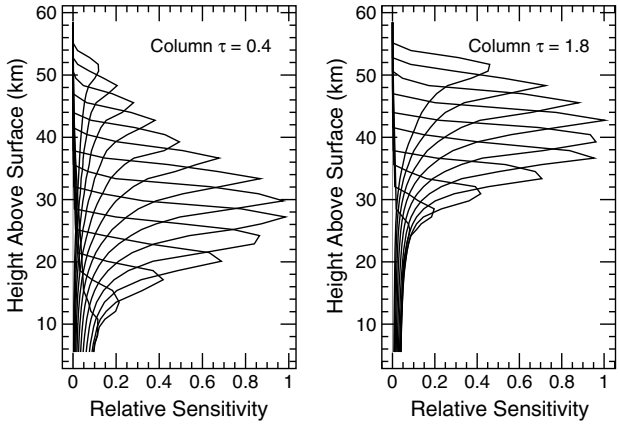

Figure 7. The relative sensitivity of observed signal to aerosol mixing ratio as a function of height for typical (left) low-dust and (right) high-dust loading cases. Each curve represents the computed change in observed signal for an incremental change in dust mixing ratio in a single model layer. The vertical range over which the retrieval is sensitive is shown by the amplitude of the curves. There is no sensitivity to near-surface aerosol when column optical depth is high.

vertical range (25 km or higher in the example shown with column optical depth greater than unity). For each retrieval, the sensitivity functions are computed and used to determine the vertical range over which there is sensitivity to the aerosol profile, and only those values are kept and reported here. The width and overlap of these curves also allow for an estimate of the vertical resolution of the retrieved profiles, which we estimate as 5 km.

[27] Figure 8 shows the best-fit computed radiance to the same observed CRISM limb scan as shown previously in Figure 3. The quality (root-mean-square (rms) difference between observed and best fit radiance) of this fit is good. The retrieved vertical profiles for dust and water ice aerosols show that dust is nearly well mixed below about 25 km and falls off rapidly above that level. A discrete water ice cloud

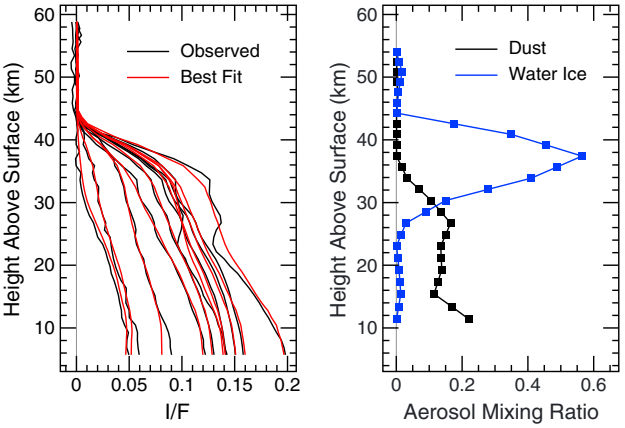

Figure 8. (left) An example of a model fit (red line) to the observations (black line) for a single limb scan (same shown as in Figure 3; MY 29, $L_s = 301°$, 19°S latitude, 290°W longitude). Each curve represents one of the ten wavelengths used in the retrieval. (right) The corresponding retrieved dust and water ice aerosol vertical profiles.

forms in a layer centered at a height of about 38 km, capping the dust distribution. Although the water ice cloud has much higher peak mixing ratio than the dust, it is located much higher above the surface where there is less atmospheric mass and is confined to about a scale height in thickness so that the total integrated column optical depth of the water ice cloud is 0.35 compared to the integrated dust optical depth of 0.38 (extrapolating the lowest retrieved dust mixing ratio to the surface).

3.3. Uncertainties

[28] Because of the large amount of spatial averaging parallel to the limb, the formal uncertainties calculated by propagation of instrument noise are relatively small except near the top of the retrieval domain where the observed signal goes to zero. The height at which the observed signal becomes small depends on a number of factors including season, illumination geometry, and the amount and distribution of aerosols, but in most cases, there is appreciable signal to at least 40–50 km. Also of relevance are the uncertainties related to systematic errors in the assumptions and approximations used in the retrieval process. These uncertainties are difficult to evaluate and are best estimated by numerical experiment.

[29] Model-related assumptions, such as the number of vertical levels used to model the atmosphere, the number of streams used in the discrete ordinates, and the number of terms used in the Legendre polynomial expansion of the aerosol scattering phase function were tested by (for example) doubling the number of levels, streams, or terms in the expansion. All of these resulted in changes in retrieved abundances of less than 2%. Use of the pseudo-spherical approximation for the limb scattering also results in small errors (recall Figure 6).

[30] Perhaps the largest source of uncertainty is the assumption of a single set of scattering properties for the dust aerosols and a (different) single set of scattering properties for the water ice aerosols for all seasons and locations. This implies a uniform composition and particle size distribution for each of the two aerosol types. While previous studies have shown variations in particle size with season and location [e.g., *Wolff and Clancy*, 2003; *Clancy et al*., 2003; *Wolff et al*., 2006, 2009], numerical experiments show that these variations serve primarily to alter the relative amplitude (or mixing ratio) of features through changes in the extinction coefficient as a function of wavelength and that they do not change the overall character of aerosol vertical profiles. When a particle size for a given aerosol (dust or water ice) is used that does not fit the observations well, an artifact can arise in the retrieved abundance of the other aerosol. For example, using a water ice particle size that is "wrong" such that it does not fit the observations well can introduce an artifact in the retrieved dust profile at the locations of prominent water ice clouds. On the basis of numerical experiments using a range of effective particle sizes for dust and water ice aerosols, we found that using an effective particle radius of $r_{\mathrm{eff}} = 1.5\,\mu$m for dust and $r_{\mathrm{eff}} = 2.0\,\mu$m for water ice aerosols gave the best fits (lowest residual between computed and observed radiance) and fewest artifacts in a global sense.

[31] An overall uncertainty in the retrieved dust and water ice mixing ratio was estimated numerically as the increment in mixing ratio that produces a corresponding difference in computed radiance that is equal to the average rms radiance difference between observed and best-fit solutions. Figure 9 shows this estimate, which is the same for dust and water ice mixing ratio at 2219 nm. The retrieval has best sensitivity (and lowest uncertainty) between an altitude of about 15 and 30 km, and uncertainties increase at the highest and lowest altitudes. An uncertainty of 0.05 in the mixing ratio corresponds to a fractional uncertainty of roughly 10% for prominent clouds.

4. Results

[32] Here we present the results of retrievals of dust and water ice aerosol vertical profiles from the CRISM limb sets. All of the limb scans for a particular limb set are combined to show the results in cross-section form as a function of latitude and height above the surface. Only those limb scans taken during daylight with a solar incidence angle $<85°$ are shown. All retrieval results are shown in terms of the mixing ratio described earlier at a reference wavelength of 2219 nm.

4.1. Typical Aerosol Cross Sections

[33] The retrieved results from July 2009 (MY 29, $L_s = 301°$) shown in Figure 10 reveal a moderately dusty atmosphere with column-integrated dust optical depths of 0.3–0.5 at low latitudes. Significant vertical structure is apparent at nearly all latitudes. The "top" of the dust distribution is at about 30–40 km above the surface between 50°S and 30°N latitude but drops to about 25 km over the summer (southern) high latitudes and to about 10–15 km over the winter (northern) mid and high latitudes. The mixing ratio of dust appears to be somewhat depressed below the main low-latitude water ice clouds. The layers of dust above the main haze in the north that are associated with high water ice clouds may be artifacts indicative of an ice particle size different than the assumed $r_{\mathrm{eff}} = 2.0\,\mu$m at those locations.

[34] Water ice aerosols are almost completely confined to layers at high altitudes, often capping the dust layer as also observed by *Kleinböhl et al*. [2009]. A low-latitude water

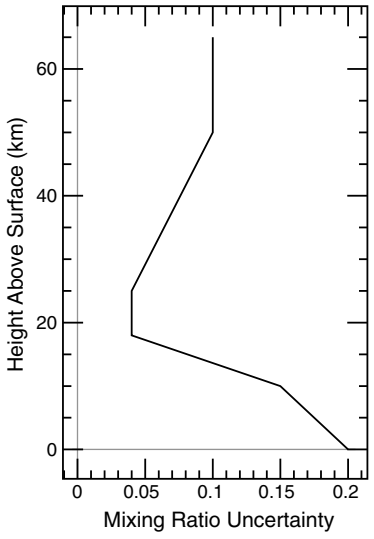

Figure 9. The total estimated uncertainty in retrieved dust and water ice aerosol mixing ratio at 2219 nm as a function of height above the surface.

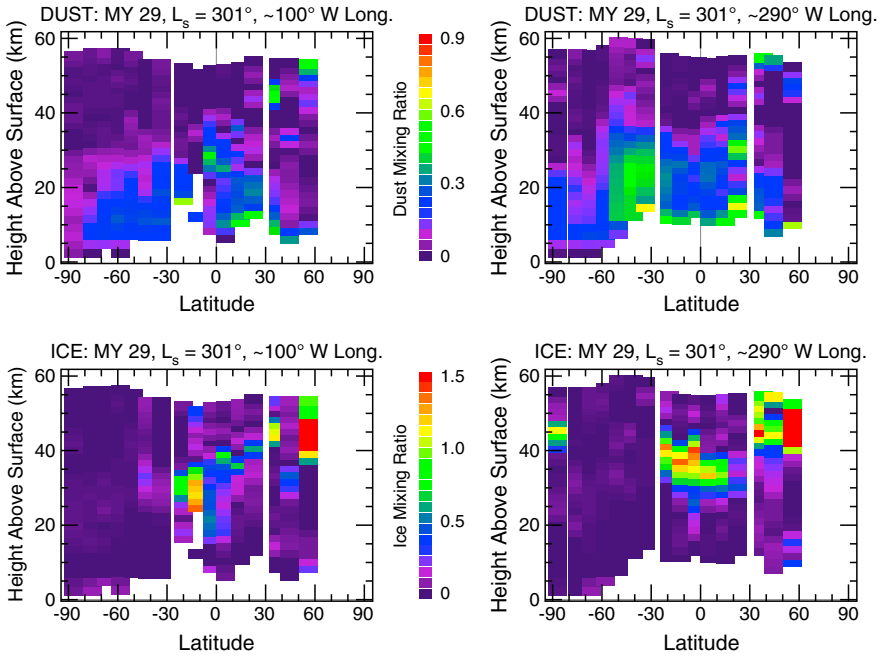

Figure 10. Retrieved cross sections of (top) dust and (bottom) water ice for the limb set taken in July 2009 (MY 29, $L_s = 301°$). (left) Retrievals from the orbit near 100°W longitude. (right) Retrievals from the orbit near 290°W longitude.

ice cloud between 30 and 40 km above the surface was present between 30°S and 20°N latitude, while a separate group of clouds was present at 40–55 km above the surface at mid-northern latitudes. A single isolated cloud at 45 km altitude was observed near the south pole in one orbit, but not in the other.

[35] Figure 11 shows the retrieved results from the most recent limb set taken in April 2012 (MY 31, $L_s = 102°$), the opposite season as shown in Figure 10. At this time, there was much less dust, but there was a prominent water ice cloud at low latitudes. The small amount of dust that is observed was confined below 20 km at all latitudes with

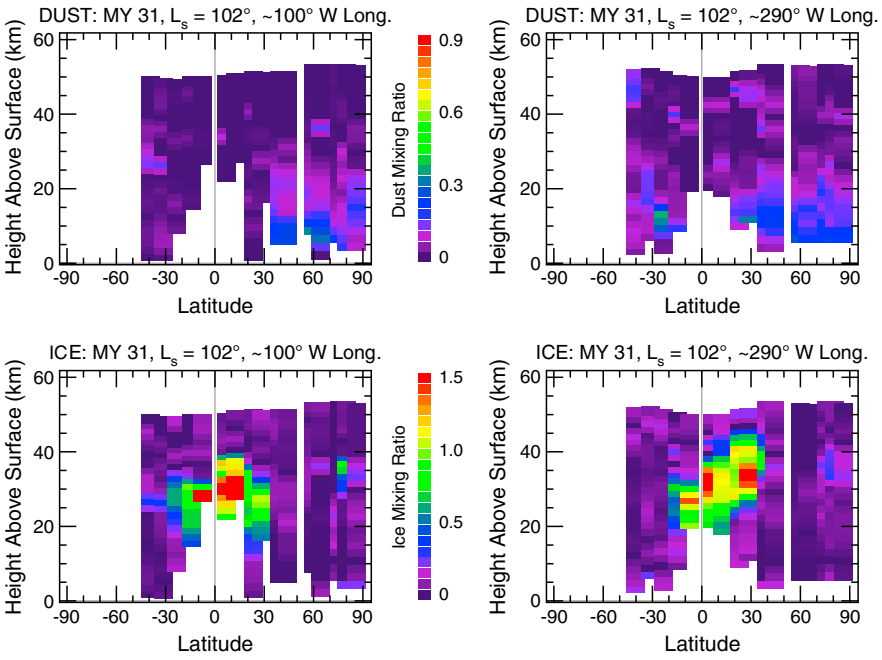

Figure 11. Retrieved cross sections of (top) dust and (bottom) water ice for the limb set taken in April 2011 (MY 31, $L_s = 102°$). (left) Retrievals from the orbit near 100°W longitude. (right) Retrievals from the orbit near 290°W longitude.

highest opacity near the summer (north) pole. A well-formed low-latitude water ice cloud extended from 20°S to 30°N latitude and had a vertical depth of about 10 km. The height of the cloud varied systematically with the latitude, with the cloud located between 20 and 30 km at 20°S latitude and gradually becoming higher to the north reaching an altitude of 35–45 km at its northernmost extent at 30°N latitude. An isolated water ice cloud above the summer (north) polar region at 80°N latitude and 35 km altitude mirrors the similar isolated water ice cloud observed over the summer (south) pole in July 2009 (Figure 10).

[36] The two longitudes observed for each CRISM limb set allow for a rough comparison of longitude variability, which is enhanced by the strong topographic differences between the two observed longitudes (Tharsis at 100°W longitude vs. Syrtis Major and Hellas at 290°W longitude), and indeed, although the overall distribution between the two longitudes is often similar, retrieved aerosol cross sections do show differences in the vertical structure that are often associated with topography. In the case from MY 29, $L_s = 301°$, there is a significant enhancement of dust over Hellas basin (30°S–50°S latitude, 290°W longitude), with dust also extending to a higher altitude above the surface. In the case from MY 31, $L_s = 102°$, the differences are more minor, confined primarily to the structure of the low-latitude water ice cloud.

4.2. Variation With Season

[37] A sampling of the seasonal dependence of dust and water ice aerosol cross sections retrieved from CRISM limb sets is shown in Figures 12 and 13. As expected [e.g., *Smith*, 2008, and references therein], there is significantly more dust overall during the perihelion season ($L_s = 180–360°$) than during the aphelion season ($L_s = 0–180°$). The dust typically extends to a height of about 40 km above the surface when significant dust is present and is confined within 10–20 km of the surface when the column-integrated optical depth of dust is low (aphelion season and winter high latitudes). Although all seasons show significant departures from well-mixed profiles, the equinoctal seasons tend to show the most structure in the vertical distribution of dust and appear to be transitional times between the "dusty" and more "clear" seasons.

[38] In these cross sections that are all taken at 290°W longitude, there is consistently enhanced dust over Hellas (30°S–50°S latitude), with dust extending to higher altitudes and showing greater vertical structure than in neighboring latitudes. The cross sections at 100°W longitude (not shown) show similar trends, except without the Hellas enhancement and typically slightly less dust overall.

[39] Water ice clouds (Figure 13) are present in all seasons but are most extensive around the northern hemisphere summer solstice, when they extend much closer to the surface and have column optical depths that can approach unity at 2219 nm. Clouds are often observed to cap the main dust layer, but there are exceptions. Clouds are observed almost always as discrete layers, typically 5–10 km in depth, with base levels as low as 20 km above the surface at low latitudes during the northern hemisphere summer season and as high as 40–50 km above the surface for isolated clouds at mid latitudes in all seasons. It is likely that water ice clouds also form near the surface at winter high latitudes where CRISM cannot observe because of lack of sunlight. At the equinoxes, there is some indication of low-altitude clouds at the most poleward latitudes.

[40] Water ice clouds show more variation between the two longitudes observed than does dust. In general, the water ice clouds retrieved from the orbit at 100°W longitude (Tharsis) are systematically lower by 5–10 km and appear more disorganized with greater vertical structure than the clouds retrieved from the orbit at 290°W longitude (Syrtis Major and Hellas). There also tend to be more clouds with somewhat higher column optical depth in the Tharsis orbit (see Figures 10 and 11 for examples). In the one limb set (MY 31, $L_s = 102°$) that contains a third orbit at 0° longitude (Meridiani Planum), the clouds in the Meridiani orbit appear more like those in the Syrtis/Hellas orbit than those in the Tharsis orbit.

4.3. Repeatability

[41] As CRISM works through its second Martian year of limb observations, we can now begin to examine the repeatability of the aerosol cross sections from one Martian year to the next. Figures 14 and 15 show two examples at different seasons, with both cases showing the longitude near 290°W. The late perihelion season is shown in Figure 14, when there is still a relatively large amount of dust in the atmosphere (although neither MY 29 nor MY 30 was a year with a planet-encircling dust storm). There are differences in the details, but the overall pattern for both dust and water ice is similar. In both MY 29 and MY 30, dust extended to about 35–40 km in height between 50°S and 30°N latitude with an abrupt drop to 25–30 km poleward of 60°S, and in both years, there was a significant enhancement of dust over Hellas with the top of the dust layer extending to nearly 50 km. A water ice cloud capped the dust at a 35–45 km altitude between 20°S and 20°N latitude in both Martian years with disorganized higher altitude clouds poleward of 30°N. The isolated cloud near the south pole observed in MY 29 was not present in MY 30.

[42] Aphelion season cross sections (Figure 15) taken one Martian year apart also show close correspondence. There is little dust observed on this season ($L_s \approx 100°$) in either MY 30 or MY 31, and what is observed is confined below a 20 km altitude and primarily in the northern hemisphere. The low-latitude aphelion-season cloud belt dominates the water ice aerosol cross section for both years, with its characteristic "tilt" toward a higher altitude at more northerly latitudes.

[43] Both of these examples represent nominal cases. Of course, during large dust storms, we would expect significant variations in the retrieved cross sections. With luck, a future CRISM limb set will catch an active planet-encircling dust storm in progress.

5. Discussion

5.1. Comparison With Mars Climate Sounder Observations

[44] The MCS instrument [*McCleese et al.*, 2007] on board MRO also retrieves vertical profiles of dust and water ice aerosols [*Kleinböhl et al.*, 2009, 2011; *McCleese et al.*, 2010]. The MCS retrievals were performed on observations taken in the thermal infrared (12–22 μm), while the CRISM retrievals use near-infrared (1.2–3.7 μm) observations. Although exactly

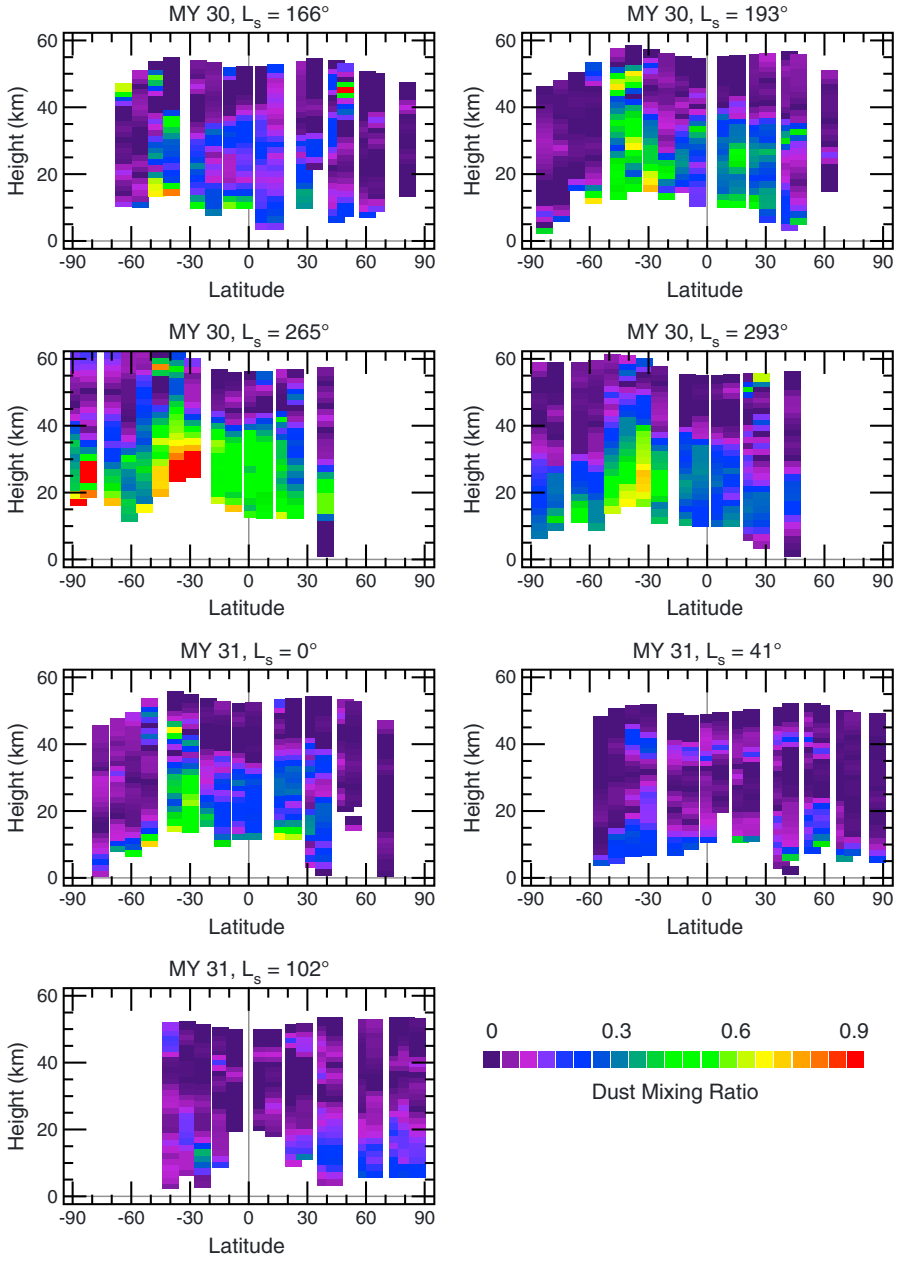

Figure 12. Cross sections showing the seasonal variation of dust vertical and latitudinal distributions. All retrievals are from orbits near 290°W longitude.

simultaneous observations between MCS and CRISM are not possible because the MRO spacecraft must be pitched away from its normal nadir orientation for CRISM to observe the limb, it is still possible and instructive to compare nearly simultaneous observations. In general, MCS observes the forward limb while CRISM observes the aft limb during the same orbit, such that both instruments observe a similar part of the atmosphere within about 15 min.

[45] Figure 16 shows one such comparison for the CRISM limb set taken in October 2010 (MY 30, $L_s = 166°$) for the orbit near 290°W longitude. Figure 16 (top) shows the dust (left) and water ice (right) cross sections retrieved from CRISM, while the bottom shows the dust and water ice cross sections retrieved from MCS. The mixing ratios have been scaled to a common wavelength reference (2219 nm) for ease of comparison. Overall, the two instruments produce similar results. Although there was not much dust in the atmosphere at this time, both instruments showed an enhancement in dust over Hellas (30°S–50°S latitude) with the dust extending to higher altitudes above the surface in that region. The correspondence between the retrieved water ice clouds is even more striking. In the south, there is a low-level enhancement below 20 km and poleward of 50°S latitude and isolated clouds at 35 km, 40°S and at 48 km, 50°S. A higher cloud near 60 km, 40°S latitude observed by MCS is beyond the retrieval range of CRISM. In the north, a line of clouds is observed by both instruments that begins about 30 km above the surface at 35°N latitude and extends upward and poleward to about 45 km altitude at 50°N. Poleward of those clouds, both instruments observe a general weak enhancement in water

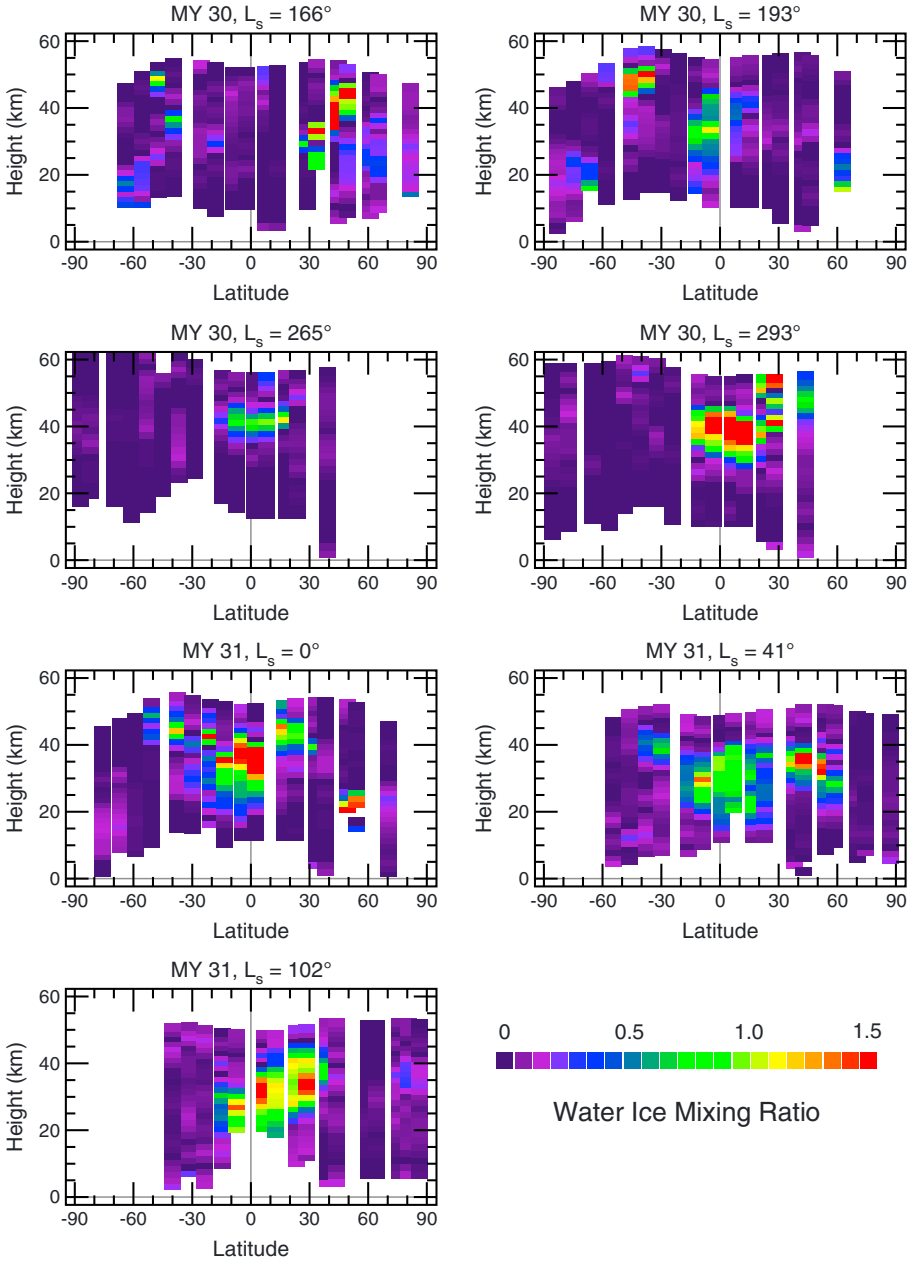

Figure 13. Cross sections showing the seasonal variation of water ice vertical and latitudinal distributions. All retrievals are from orbits near 290°W longitude.

ice mixing ratio over a broad range of altitudes. The isolated dust clouds at 35–50 km at mid-northern and southern latitudes in the CRISM cross section are likely artifacts as they align with strong water ice clouds.

[46] One of the most striking features of the MCS retrievals is the so-called *high-altitude tropical dust maximum* (HATDM), which is the local maxima in the dust mixing ratio commonly observed over the tropics during the northern spring and summer seasons at altitudes of 15–25 km [*Heavens et al.*, 2011]. Figure 17 shows a case where the HATDM was observed in simultaneous observations by CRISM and MCS (MY 30, $L_s = 193°$, orbit near 290°W longitude). In this case, the HATDM shows up as a clear maximum in the dust mixing ratio between 20°N and 45°N latitude at a height of 25–30 km above the surface. The dust layer is no more than 5 km thick and contains a dust mixing ratio several times larger than immediately above or below it, especially at its northernmost extent. More detached dust clouds are apparent above Hellas (35°S–50°S latitude) in both the CRISM and MCS retrievals. The HADTM is present in some other CRISM retrievals (e.g., the MY 31, $L_s = 0°$ case shown in Figure 12 at 30°N latitude and 30 km altitude), but it is not prominent in many CRISM retrievals. However, in the MCS data set, the HADTM appears much more frequently in retrievals using nighttime observations than in those using daytime observations [*Heavens et al.*, 2011], and in the (daytime only) simultaneous MCS and CRISM observations, whenever the HADTM is observed in the MCS retrievals, it is also observed in the CRISM retrievals. Comparisons of other CRISM limb sets with nearly simultaneous MCS retrievals show similar correspondence.

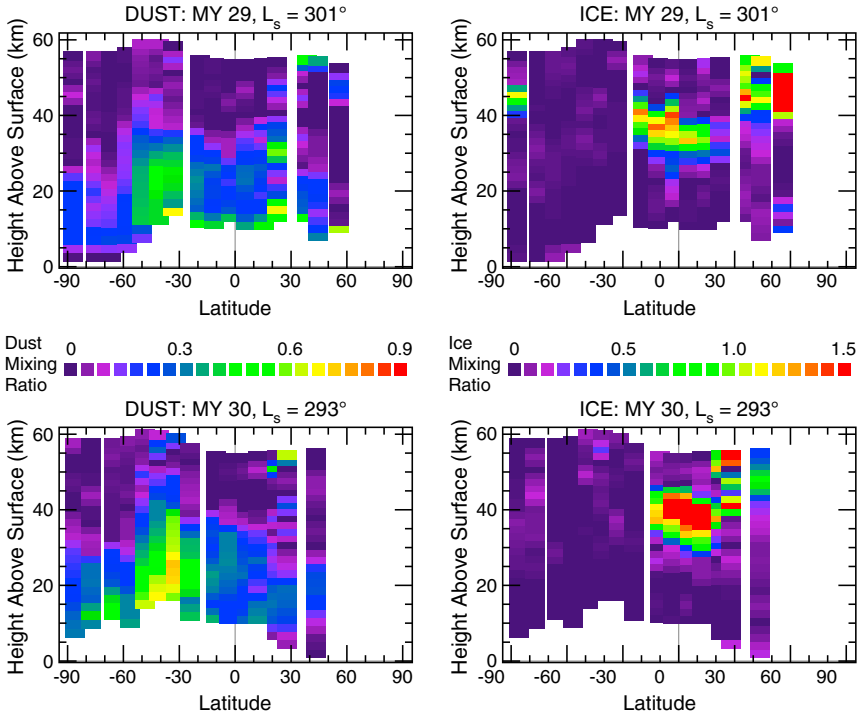

Figure 14. A comparison of (left) dust and (right) water ice cross sections retrieved from CRISM limb sets taken one Martian year apart during the perihelion season ((top) MY 29, $L_s = 301°$ and (bottom) MY 30, $L_s = 293°$). All retrievals are from orbits near 290°W longitude.

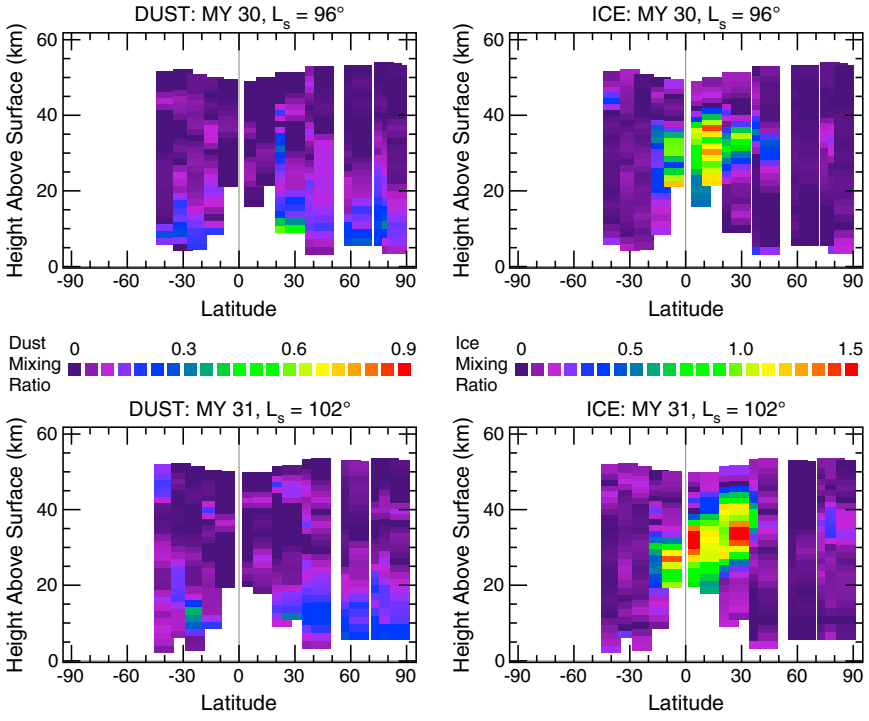

Figure 15. A comparison of (left) dust and (right) water ice cross sections retrieved from CRISM limb sets taken one Martian year apart during the aphelion season ((top) MY 30, $L_s = 96°$ and (bottom) MY 31, $L_s = 102°$). All retrievals are from orbits near 290°W longitude.

5.2. Modeling Aerosol Vertical Distributions

[47] In the same way that many previous retrievals from observational data used the simplifying assumption of a well-mixed aerosol (especially for dust), most general circulation model (GCM) simulations of the Mars atmosphere have also assumed simplified expressions for the vertical

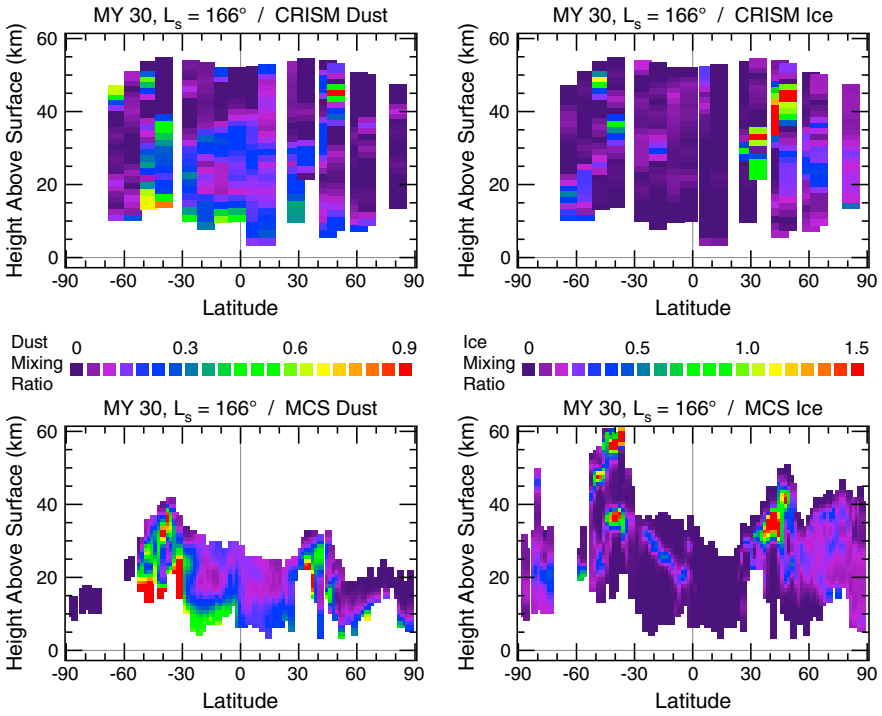

Figure 16. A comparison of (left) dust and (right) water ice cross sections retrieved from nearly simultaneous (top) CRISM and (bottom) MCS observations taken in October 2010 (MY 30, $L_s = 166°$). All retrievals are near 290°W longitude, and the mixing ratios have been scaled to a common wavelength reference.

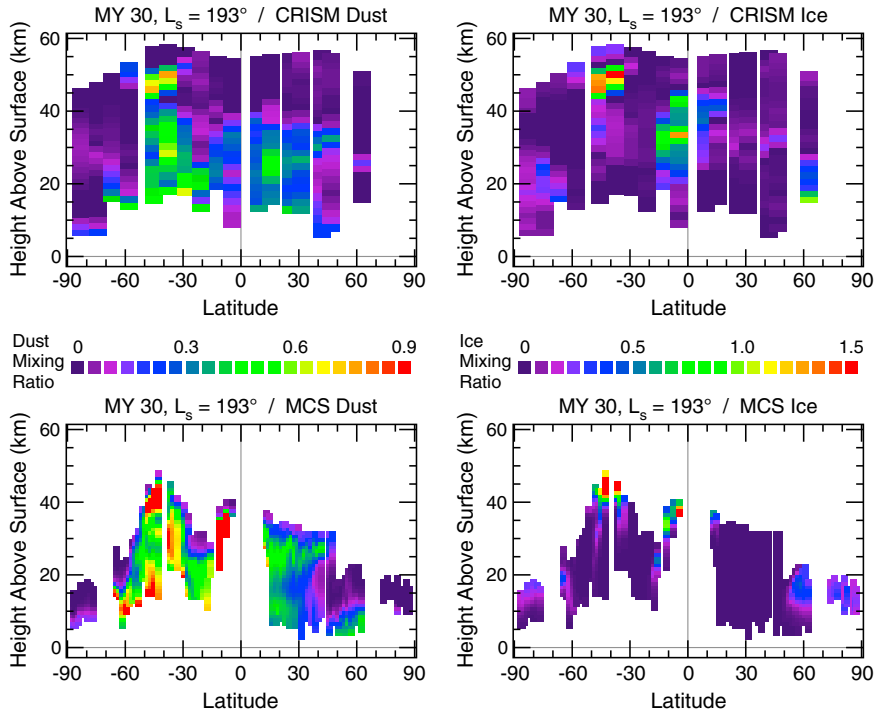

Figure 17. A comparison of (left) dust and (right) water ice cross sections retrieved from nearly simultaneous (top) CRISM and (bottom) MCS observations taken in December 2010 (MY 30, $L_s = 319°$). All retrievals are near 290°W longitude, and the mixing ratios have been scaled to a common wavelength reference.

distribution of aerosol. By far, the most common is the Conrath-v vertical profile for dust [*Conrath*, 1975]. This approximation uses a single parameter, v, to set the relative balance between gravitational settling and vertical mixing by eddies. The resulting profile is nearly well mixed at the bottom before rapidly falling off to zero at a height determined by the value of v. This approximation found wide acceptance because of its computational efficiency, its basis on physical phenomena, and the lack of observations to provide other information. A few investigations [*Murphy et al*., 1993; *Wilson and Hamilton*, 1996; *Newman et al*., 2002; *Basu et al*., 2004; *Kahre et al*., 2006, 2008] have allowed dust to be actively transported by model-generated winds; however, these simulations produced dust vertical profiles that did not differ significantly from the Conrath-v parameterization.

[48] However, retrievals from the TES, MCS, and now CRISM limb observations clearly show that a Conrath-v parameterization for the vertical distribution of dust is not a good approximation, and because of this, recent efforts by *Guzewich et al.* [2011], *Richardson et al.* [2011], and *Rothchild et al*. [2011] have begun to investigate the effect of more realistic dust vertical profiles in GCM models. *Guzewich et al*. [2011] find that the inclusion of observed high-altitude dust layers in their GCM model results in a significant improvement in the intensity and location of the polar warming over that obtained using the Conrath-v parameterization. The continued collection of limb-geometry observations, including that by CRISM, will provide the necessary data for further improvement of GCM models enabling a better understanding of Mars atmospheric phenomena.

5.3. Particle Size Retrieval

[49] The overall agreement between the CRISM and MCS retrievals serves as a validation of the algorithms used for both retrievals although differences in the retrieved quantities can also be diagnostic. In particular, the ratio of aerosol optical depth at visible or near-infrared (CRISM) to aerosol optical depth at thermal infrared (MCS) wavelengths is sensitive to aerosol particle size [e.g., *Clancy et al*., 2003; *Wolff et al*., 2006] over a wide range of particle sizes from submicron to tens of microns. Particle size directly contributes to the radiative properties of aerosols, including their extinction cross section and single-scattering albedo, and also plays a role in particle microphysics. The gravitational settling time for aerosols is a strong function of particle size, which constrains the mechanisms that can create and maintain the observed vertical structure.

[50] A full analysis of the particle sizes implied by the combination of CRISM and MCS retrievals is beyond the scope of this work. However, a quick comparison of the retrieval results displayed in Figures 16 and 17 shows that the mixing ratios agree well for both dust and water ice, indicating that the assumed mean particle sizes are reasonable for this season. In this way, the CRISM limb observations contribute key complementary information to the MCS limb observations, and a complete retrieval of aerosol particle size as a function of season, latitude, and height is a priority for future work.

6. Summary

[51] Visible and near-infrared spectra taken by CRISM in the limb-viewing geometry enable the retrieval of the vertical profile of dust and water ice aerosols. Both dust and water ice vertical profiles often show significant vertical structure for nearly all seasons and latitudes that are not consistent with the well-mixed or Conrath-v assumptions that have often been used in the past for describing aerosol vertical profiles for retrieval and modeling purposes. The CRISM limb-geometry observations also include other important spectral features that enable the detailed study of other atmospheric phenomena such as O_2 airglow [*Clancy et al*., 2012], and water vapor and CO gas abundance [*Smith et al*., 2011].

[52] With the collection of more than a dozen CRISM limb sets covering all Martian seasons, the CRISM limb observations reveal many aspects of the vertical distribution of aerosols and their seasonal and spatial dependence. The amount of dust and its vertical extent are observed to vary greatly with season, with the horizontal distribution generally following the known climatology. During the perihelion season, the column-integrated optical depth is high, and dust is mixed to 40–50 km above the surface at low latitudes, but only to about 30 km at high southern (summer) latitudes. During the perihelion season, the much smaller amount of dust that is present is largely confined below 20 km altitude with more dust in the northern hemisphere. Spatial variations are also observed, with a persistent enhancement of dust over Hellas in most seasons (but especially in the equinox seasons) where dust has both a significantly higher mixing ratio and is mixed to higher altitudes than at neighboring latitudes or at a different longitude.

[53] Water ice aerosol is also observed to show large seasonal and spatial variations. Water ice aerosols were observed almost exclusively in the form of detached clouds, often capping the dust distribution. Significant water ice clouds were observed in all seasons although clouds tended to have higher column optical depth, had lower base altitudes, and extended over a greater vertical range during the aphelion season, as expected. The low-latitude aphelion season cloud belt is observed to have a characteristic "tilt" with a lower vertical range at its southern extent (17–33 km at 20°S latitude) than at its northern extent (25–45 km at 30°N latitude), a trait not previously described. Water ice clouds, in general, appeared more disorganized and appeared to have greater vertical structure at the longitude over Tharsis than at the longitude over Syrtis Major and Hellas.

[54] The CRISM limb observations nicely complement those taken by MCS. Comparison of latitude-height cross sections of retrieved aerosol mixing ratios from nearly simultaneous CRISM and MCS limb observations show an overall good correspondence validating both the CRISM and MCS retrieval algorithms through an independent confirmation of results. In particular, the HATDM, discovered in MCS observations, is also observed by CRISM whenever it is apparent in the MCS retrievals. Additional analysis of the combination of CRISM and MCS retrievals have the potential

to provide useful constraints on aerosol particle sizes because of the different wavelengths used by the two instruments.

[55] As of this writing, CRISM continues to collect new data in both the nominal nadir-viewing and the occasional limb-viewing geometries. Continued observations will be useful for characterizing interannual variations, especially during large dust storms.

[56] **Acknowledgments.** The authors acknowledge financial support from the NASA Mars Reconnaissance Orbiter project as members of the CRISM and MCS Science Teams and are grateful for all the hard work done by the CRISM operations team at the Applied Physics Laboratory who performed all the sequencing and calibration needed to obtain this data set. All data products used as input to the retrieval process as well as all output results are available from the author upon request. We thank Scott Guzewich for a helpful discussion of this work, and we appreciate the review comments from Mark Richardson and an anonymous referee.

References

Anderson, E., and C. Leovy (1978), Mariner 9 television limb observations of dust and ice hazes on Mars, *J. Atmos. Sci.*, *35*, 723–734.

Basu, S., M. I. Richardson, and R. J. Wilson (2004), Simulation of the Martian dust cycle with the GFDL Mars GCM, *J. Geophys. Res.*, *109*, doi:10.1029/2004JE002243.

Berk, A. L., S. Bernstein, G. P. Anderson, P. K. Acharya, D. C. Robertson, J. H. Chetwynd, and S. M. Adler-Golden (1998), MODTRAN cloud and multiple scattering upgrades with application to AVIRIS, *Remote Sens. Environ.*, *65*, 367–375.

Cantor, B. A. (2007), MOC observations of the 2001 Mars planet-encircling dust storm, *Icarus*, *186*, 60–96.

Chassefière, E., J. E. Blamont, V. A. Krasnopolsky, O. I. Korablev, S. K. Atreya, and R. A. West (1992), Vertical structure and size distributions of Martian aerosols from solar occultation measurements, *Icarus*, *97*, 46–69.

Clancy, R. T., M. J. Wolff, and P. R. Christensen (2003), Mars aerosol studies with the MGS-TES emission phase function observations: Optical depths, particle sizes, and ice cloud types versus latitude and solar longitude, *J. Geophys. Res.*, *108*, doi:10.1029/2003JE002058.

Clancy, R. T., M. J. Wolff, B. A. Whitney, B. A. Cantor, M. D. Smith, and T. H. McConnochie (2010), Extension of atmospheric dust loading to high altitudes during the 2001 Mars dust storm: MGS TES limb observations, *Icarus*, *207*, 98–109.

Clancy, R. T., et al. (2012), Extensive MRO CRISM observations of 1.27 μm O_2 airglow in Mars polar night and their comparison to MRO MCS temperature profiles and LMD GCM simulations, *J. Geophys. Res.*, doi:10.1029/2011JE004018.

Conrath, B. J. (1975), Thermal structure of the Martian atmosphere during the dissipation of the dust storm of 1971, *Icarus*, *24*, 36–46.

Gierasch, P. J., and R. M. Goody (1972), The effect of dust on the temperature of the Mars atmosphere, *J. Atmos. Sci.*, *29*, 400–402.

Goody, R. M., and Y. L. Yung (1989), Atmospheric Radiation: Theoretical Basis, Oxford University Press, New York.

Guzewich, S. D., E. R. Talaat, A. D. Toigo, T. H. McConnochie, and D. W. Waugh (2011), Analysis of tides in a MarsWRF simulation forced with TES limb dust observations, Abstract P21A-1637, American Geophysical Union, Fall Meeting 2011, San Francisco, California.

Heavens, N. G., M. I. Richardson, A. Kleinböhl, D. M. Kass, D. J. McCleese, W. Abdou, J. L. Benson, J. T. Schofield, J. H. Shirley, and P. M. Wolkenberg (2011), Vertical distribution of dust in the Martian atmosphere during northern spring and summer: Observations by the Mars Climate Sounder and analysis of zonal average vertical dust profiles, *J. Geophys. Res.*, *116*, doi:10.1029/2010JE003691.

Jaquin, F., P. J. Gierasch, and R. Kahn (1986), The vertical structure of limb hazes in the Martian atmosphere, *Icarus*, *68*, 442–461.

Kahre, M. A., J. R. Murphy, and R. M. Haberle (2006), Modeling the Martian dust cycle and surface dust reservoirs with the NASA Ames general circulation model, *J. Geophys. Res.*, *111*, doi:10.1029/2005JE002588.

Kahre, M. A., J. L. Hollingsworth, R. M. Haberle, and J. R. Murphy (2008), Investigations of the variability of dust particle sizes in the Martian atmosphere using the NASA Ames General Circulation Model, *Icarus*, *195*, 576–597.

Kleinböhl, A., et al. (2009), Mars Climate Sounder limb profile retrieval of atmospheric temperature, pressure, dust and water ice opacity, *J. Geophys. Res.*, *114*, doi:10.1029/2009JE003358.

Kleinböhl, A., J. T. Schofield, W. A. Abdou, P. G. J. Irwin, and R. J. de Kok (2011), A single-scattering approximation for infrared radiative transfer in limb geometry in the Martian atmosphere, *J. Quant. Spect. Rad. Transf.*, *112*, 1568–1580.

McCleese, D. J., et al. (2007), Mars Climate Sounder: An investigation of thermal and water vapor structure, dust and condensate distributions in the atmosphere, and energy balance in the polar regions, *J. Geophys. Res.*, *112*, doi:10.1029/2006JE002790.

McCleese, D. J., et al. (2010), Structure and dynamics of the Martian lower and middle atmosphere as observed by the Mars Climate Sounder: Seasonal variations in zonal mean temperature, dust, and water ice aerosol, *J. Geophys. Res.*, *115*, doi:10.1029/2010JE003677.

McConnochie, T. M., and M. D. Smith (2008), Vertically resolved aerosol climatology from Mars Global Surveyor Thermal Emission Spectrometer (MGS-TES) limb sounding. Third International Workshop on the Mars Atmosphere: Modeling and Observations, Williamsburg, Virginia.

Montmessin, F., E. Quémerais, J. L. Bertaux, O. Korablev, P. Rannou, and S. Lebonnois (2006), Stellar occultations at UV wavelengths by the SPICAM instrument: Retrieval and analysis of Martian haze profiles, *J. Geophys. Res.*, *111*, doi:10.1029/2005JE002662.

Murchie, S., et al. (2007), Compact Reconnaissance Imaging Spectrometer for Mars (CRISM) on Mars Reconnaissance Orbiter (MRO), *J. Geophys. Res.*, *112*, E05S03, doi:10.1029/2006JE002682.

Murchie, S., et al. (2009), Compact Reconnaissance Imaging Spectrometer for Mars investigation and data set from the Mars Reconnaissance Orbiter's primary science phase, *J. Geophys. Res.*, *114*, E00D07, doi:10.1029/2009JE003344.

Murphy, J. R., R. M. Haberle, O. B. Toon, and J. B. Pollack (1993), Martin global dust storms: Zonally symmetric numerical simulations including size-dependent particle transport, *J. Geophys. Res.*, *98*, 3197–3220.

Newman, C. E., S. R. Lewis, P. L. Read, and F. Forget (2002), Modeling the Martian dust cycle: 2. Multiannual radiatively active dust transport simulations, *J. Geophys. Res.*, *107*, doi:10.1029/2002JE001920.

Press, W. H., S. A. Teukolsky, W. T. Vetterling, and B. P. Flannery (1992), Numerical Recipes in Fortran 77: The Art of Scientific Computing, Cambridge University Press, Cambridge.

Rannou, P., S. Perrier, J.-L. Bertaux, F. Montmessin, O. Korablev, and A. Rébérac (2006), Dust and cloud detection at the Mars limb with UV scattered sunlight with SPICAM, *J. Geophys. Res.*, *111*, doi:10.1029/2006HE002693.

Richardson, M. I., C. Lee, J. L. Anderson, N. Collins, T. J. Hoar, and W. Lawson (2011), Improved understanding of dust distribution and cap edge processes via data assimilation, Abstract P24A-06, American Geophysical Union, Fall Meeting 2011, San Francisco, California.

Rothchild, A. T., S. C. Rafkin, M. A. Kahre, and R. A. Pielke (2011), The impact of a realistic vertical dust distribution on the general circulation of the Martian atmosphere, Abstract P24A-05, American Geophysical Union, Fall Meeting 2011, San Francisco, California.

Smith, M. D. (2004), Interannual variability in TES atmospheric observations of Mars during 1999–2003, *Icarus*, *167*, 148–165.

Smith, M. D. (2008), Spacecraft observations of the Martian atmosphere, *Ann. Rev. Earth Planet. Sci.*, *36*, 191–219.

Smith, M. D. (2009), THEMIS observations of Mars aerosol optical depth from 2002–2008, *Icarus*, *202*, 444–452.

Smith, M. D., M. J. Wolff, and R. T. Clancy (2011), Vertical distribution of aerosols and water vapor using CRISM limb observations, Fourth International Workshop on the Mars Atmosphere: Modeling and Observations, Paris, France.

Spurr, R. J. D. (2002), Simultaneous derivation of intensities and weighting functions in a general pseudo-spherical discrete ordinate radiative transfer treatment, *J. Quant. Spect. Rad. Transf.*, *75*, 129–175.

Thomas, G. E., and K. Stamnes (1999), Radiative Transfer in the Atmosphere and Ocean, Cambridge Univ. Press, Cambridge, UK.

Whitney, B. A., M. J. Wolff, and R. T. Clancy (1999), Monte Carlo radiation transfer models for Mars, in Fifth International Conference on Mars, Abstract 6213, Lunar and Planet. Inst., Houston, TX.

Wilson, R. J., and K. Hamilton (1996), Comprehensive model simulation of thermal tides in the Martian atmosphere, *J. Atmos. Sci.*, *53*, 1290–1326.

Wolff, M. J., and R. T. Clancy (2003), Constraints on the size of Martian aerosols from Thermal Emission Spectrometer observations, *J. Geophys. Res.*, *104*, doi:10.1029/2003JE002057.

Wolff, M. J., et al. (2006), Constraints on dust aerosols from the Mars Exploration Rovers using MGS overflights and Mini-TES, *J. Geophys. Res.*, *111*, doi:10.1029/2006JE002786.

Wolff, M. J., R. T. Clancy, M. D. Smith, R. Arvidson, M. Kahre, F. Seelos, IV, R. V. Morris (2009), Wavelength dependence of dust aerosol single scattering albedo as observed by CRISM, *J. Geophys. Res.*, *114*, doi:10.1029/2009JE003350.

Zurek, R. W., and S. E. Smrekar (2007), An overview of the Mars Reconnaissance Orbiter (MRO) science mission, *J. Geophys. Res.*, *112*, E05S01, doi:10.1029/2006JE002701.